Alma Mater Studiorum · Università di Bologna

Scuola di Scienze
Dipartimento di Fisica e Astronomia
Corso di Laurea in Fisica

PLUME preliminary study and first Van der Meer scan data analysis

Relatore:
Prof. Angelo Carbone

Correlatore:
Dott.sa Serena Maccolini

Presentata da:
Lorenzo Nisi

Anno Accademico 2021/2022

Abstract

The Probe for LUminosity MEasurement (PLUME) detector is a luminometer for the LHCb experiment at CERN. It delivers instantaneous luminosity measurements for the upgraded LHCb detector during Run 3 at LHC. The goal of this thesis is to evaluate, with simulated data, expected performances of PLUME, such as the occupancy of the PMTs that compose the detector, and report the analysis of the first data obtained by PLUME during a Van der Meer scan. In particular, three measurements of the visible cross section, necessary to calibrate the detector, have been obtained, namely

$$\begin{aligned} \sigma_{1Da} &= (1.14 \pm 0.11)\ \text{mb}, \\ \sigma_{1Db} &= (1.13 \pm 0.10)\ \text{mb}, \\ \sigma_{2D} &= (1.20 \pm 0.02)\ \text{mb}, \end{aligned}$$

where the label $1D$ and $2D$ correspond to one-dimensional and bi-dimensional Van der Meer scan. All the results are in agreement among them.

Abstract

Il rilevatore Probe for LUminosity MEasurement (PLUME) è un luminometro per l'esperimento LHCb al CERN. Fornirà misurazioni della luminosità istantanea per LHCb durante la Run 3 a LHC. L'obiettivo di questa tesi è di valutare, con dati simulati, le prestazioni attese di PLUME, come l'occupanza dei PMT che compongono il rivelatore, e riportare l'analisi dei primi dati ottenuti da PLUME durante uno scan di Van der Meer. In particolare, sono state ottenuti tre misure del valore della sezione d'urto, necessarie per tarare il rivelatore, ovvero

$$\begin{aligned}\sigma_{1Da} &= (1.14 \pm 0.11)\ \text{mb},\\ \sigma_{1Db} &= (1.13 \pm 0.10)\ \text{mb},\\ \sigma_{2D} &= (1.20 \pm 0.02)\ \text{mb},\end{aligned}$$

dove i pedici $1D$ e $2D$ corrispondono a uno scan di Van der Meer unidimensionale e bidimensionale. Tutti i risultati sono in accordo tra loro.

Contents

Introduction

Large Hadron Collider beauty (LHCb) is an experiment at the final stage of the CERN accelerator complex, LHC. The operations at LHCb during Run 3, starting in 2022, will be subject to a significant increase in the instantaneous luminosity which is the reason for the installation of PLUME, a new luminometer.
In the first chapter, the concept of luminosity is explained. In particular, the description of luminosity in case of collision between two particle beams is analysed. The van der Meer scan, a method to evaluate the cross section of colliding beams, is also discussed at the end of this first section.
The thesis continues with a brief description of the LHCb detector and its features in the second chapter.
The structure of PLUME and its elementary detection units is discussed in chapter 3.
In the fourth and final chapter, the results of the simulation for the expected performance of PLUME are shown. The expected occupancy of PLUME detection units is studied in the case of a single layer of revealer PMTs and in the case of coincidence between two layers. After the simulation, real data from the first van der Meer scan at relatively low energies (900 GeV), is analysed. From this, it has been possible to evaluate the cross section of two colliding beams.

Chapter 1

Luminosity

Luminosity is an important quantity in particle physics that measures the ability of a particle accelerator to produce a certain number of interactions. It is the proportionality factor between the number of events per second $\mathrm{d}\mu/\mathrm{d}t$ and the cross section σ

$$\frac{\mathrm{d}\mu}{\mathrm{d}t} = \mathcal{L}\sigma, \tag{1.1}$$

luminosity depends on a variety of different factors linked to the type and geometry of the considered experiment. A brief analysis of different situations follows [1].

1.1 Fixed target collisions

In the simplest case of a beam colliding with a stationary target one can easily obtain

$$\frac{\mathrm{d}\mu}{\mathrm{d}t} = \Phi l \rho \sigma, \tag{1.2}$$

where Φ is the flux of the incoming particles from the beam, and l and ρ are the length and density of the target, respectively. In Fig. 1.1, this configuration is shown. From Eqs. 1.1 and 1.2, we can get the luminosity for a fixed target $\mathcal{L}_{FT}$

$$\mathcal{L}_{FT} = \Phi l \rho \tag{1.3}$$

. This is not the configuration used in particle accelerators. When using a pair of colliding beams, the center of mass energy is significantly higher in comparison to the one of a beam hitting a stationary target.

1.2 Colliding beams

Unlike the example of the stationary target, both beams can now be considered as target and incoming beam simultaneously. We will consider the case of colliding beams. Since

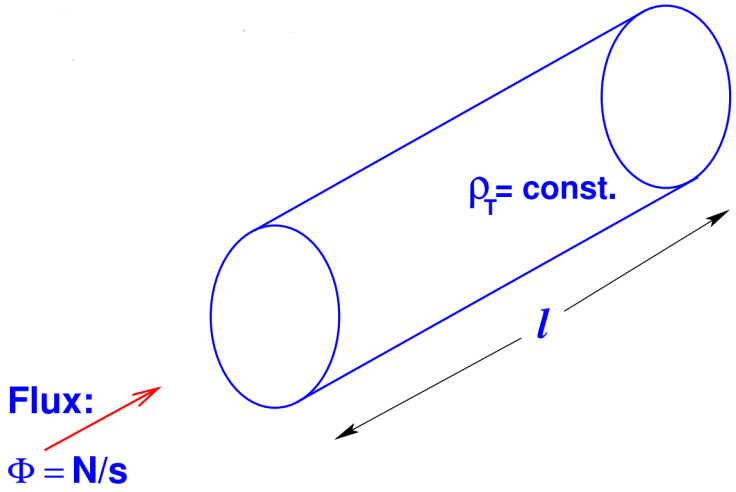

Figure 1.1: *Schematic view of a fixed target collision [1].*

the two beams are moving through each other, the overlap integral, which is proportional to the luminosity, depends on the longitudinal position of the bunches and it is therefore time-dependent. The overlap integral is defined as

$$\iiiint \rho_1(x, y, s, -s_0)\rho_2(x, y, s, s_0)\mathrm{d}x\mathrm{d}y\mathrm{d}s\mathrm{d}s_0, \tag{1.4}$$

where s is the direction in which the two beams are moving, x and y are the two perpendicular directions to s, $s_0 = ct$ is the distance of the two bunches from the central collision point which is being used as our "time" variable and ρ_1 and ρ_2 are the time dependent density distributions of the beams. In Fig. 1.2, this configuration is shown. Since the beams can move through each other at different speeds and orientations we must multiply the previous expression by a kinematic factor

$$K = \sqrt{(\vec{v_1} - \vec{v_2})^2 - \frac{(\vec{v_1} \times \vec{v_2})^2}{c^2}}. \tag{1.5}$$

In this thesis we consider only head-on collision, *i.e.* $(\vec{v_1} = -\vec{v_2})$, which implies $K = 2$. Correction due to offset a different crossing angles between the beams are discussed in the following paragraphs. Assuming the densities along different dimensions are uncorrelated, we get the following expression for the luminosity

$$\mathcal{L} = 2N_1N_2fN_b \iiiint \rho_{1x}(x)\rho_{1y}(y)\rho_{1s}(s - s_0)\rho_{2x}(x)\rho_{2y}(y)\rho_{2s}(s + s_0)\mathrm{d}x\mathrm{d}y\mathrm{d}s\mathrm{d}s_0, \tag{1.6}$$

where N_1 and N_2 are the bunches intensities, N_b is the number of bunches per beam and f is the beam revolution frequency. If we assume Gaussian profiles of the bunches for

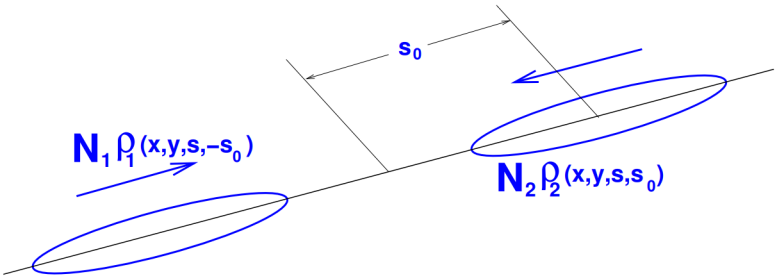

Figure 1.2: *Schematic view of a pair of colliding bunches [1].*

the density distributions and equal beams

$$\rho_z(z) = \frac{1}{\sigma_z\sqrt{2\pi}} exp(-\frac{z^2}{2\sigma_z^2})$$

where $z = x, y$, and

$$\rho_s(s \pm s_0) = \frac{1}{\sigma_s\sqrt{2\pi}} \exp(-\frac{(s \pm s_0)^2}{2\sigma_s^2}),$$

it is possible to evaluate Eq. 1.6 obtaining

$$\mathcal{L} = \frac{N_1 N_2 f N_b}{4\pi\sigma_x\sigma_y}, \tag{1.7}$$

where σ_x and σ_y are the standard deviations of the bunch Gaussian profiles.

Usually, colliding beams are not parallel and we have to consider a possible crossing angle, ϕ, between the two. In Fig 1.3, the rotated reference system of this configuration is shown.

In addition to that, the beams do not always collide head on, but with a small transverse offset. In Fig. 1.4 the reference system is translated of a distance d_1 for the first beam and a distance d_2 for the second. The resulting coordinates transformations are

$$x_1 = d_1 + x\ \cos\frac{\phi}{2} - s\ \sin\frac{\phi}{2} \qquad s_1 = s\ \cos\frac{\phi}{2} + x\ \sin\frac{\phi}{2}$$

$$x_2 = d_2 + x\ \cos\frac{\phi}{2} - s\ \sin\frac{\phi}{2} \qquad s_2 = s\ \cos\frac{\phi}{2} + x\ \sin\frac{\phi}{2}$$

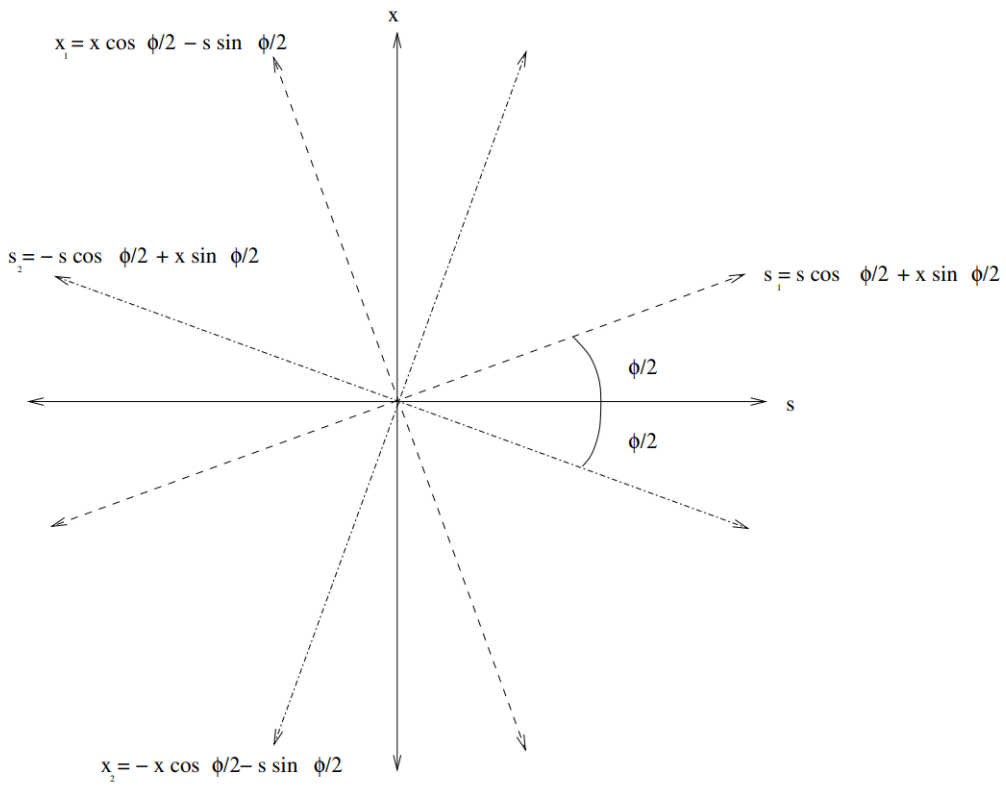

Figure 1.3: *Rotated reference system for colliding beams with a ϕ crossing angle. Each beam has been rotated of a $\phi/2$ angle in order to have a symmetrical reference system [1].*

If we now evaluate the luminosity through the overlap integral (Eq. 1.4) and the kinematic factor (Eq. 1.5), the expression for the luminosity becomes

$$L = \frac{N_1 N_2 f N_b}{4\pi\sigma_x\sigma_y} \cdot W \cdot e^{\frac{B^2}{A}} \cdot S, \tag{1.8}$$

where W, $e^{\frac{B^2}{A}}$ and S are correction factors. Namely, W is a factor that reduces the luminosity in the presence of beam offsets and has the following expression

$$W = \exp(-\frac{1}{4\sigma_x^2}(d_2 - d_1)^2), \tag{1.9}$$

and the parameter S reduces the luminosity in the presence of crossing angles and has the following expression

$$S = \frac{1}{\sqrt{1 + \frac{\sigma_s}{\sigma_x}\tan\frac{\phi}{2}}} \approx \frac{1}{\sqrt{1 + \frac{\sigma_s}{\sigma_x}\frac{\phi}{2}}}. \tag{1.10}$$

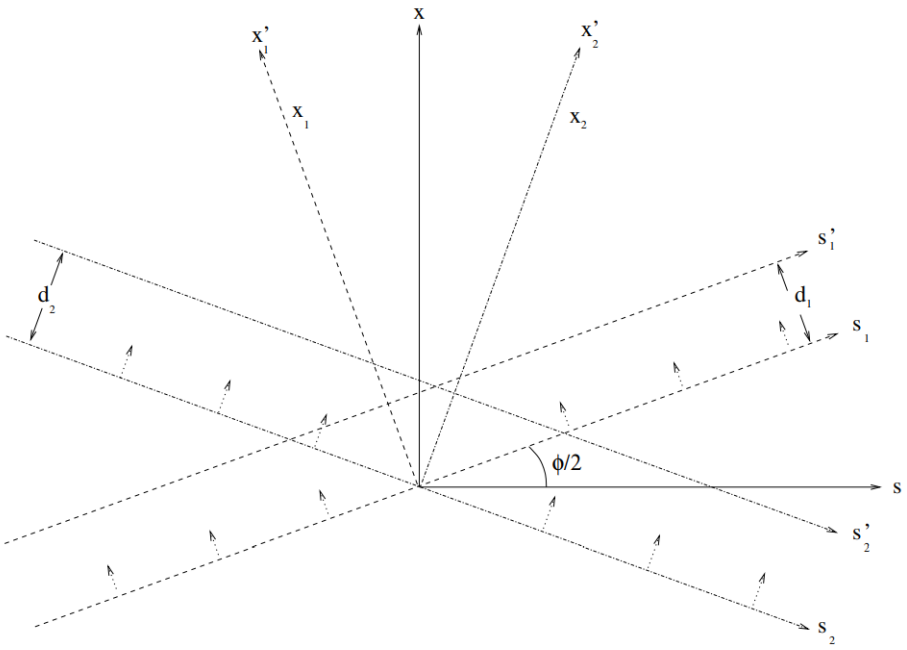

Figure 1.4: *Final reference system showing both the crossing angle and the offset between the beams [1].*

Finally, the last correction factor is only present when we have crossing angles and beam offset simultaneously. The parameters A and B can be written as

$$A = \frac{\sin^2\frac{\phi}{2}}{\sigma_x^2} + \frac{\cos^2\frac{\phi}{2}}{\sigma_s^2} \qquad B = \frac{(d_2 - d_1)\,\sin\frac{\phi}{2}}{2\sigma_x^2}. \tag{1.11}$$

It is useful to calculate the integrated luminosity, *i.e.* the luminosity integrated over time an arbitrary interval of time T, namely

$$\mathcal{L}_{int} = \int_0^T \mathcal{L}(t)\mathrm{d}t \tag{1.12}$$

From Eq. 1.1 and Eq. 1.12, it follows

$$\mu = \mathcal{L}_{int}\sigma, \tag{1.13}$$

This means that $\mathcal{L}_{int}$ is directly linked to the number of observed events, giving integrated luminosity even a greater importance in respect to instantaneous luminosity.

1.3 The Van der Meer scan

One useful method to evaluate the cross section σ and calibrate luminosity at hadron colliders is the so-called Van der Meer scan [2]. Considering the collision of two bunches with N_1 and N_2 particles travelling in opposite directions, the luminosity is reduced when the beams are separated in the transverse plane, as shown by Eq. 1.9. Thus, the number of observed interactions will change accordingly. If the separation of the bunches along the two transversal directions are Δx and Δy and it is possible to divide both members in Eq. 1.13 by $N_1 N_2$, obtaining

$$\frac{\mu(\Delta x, \Delta y)}{N_1 N_2} = \sigma \frac{\mathcal{L}_{int}}{N_1 N_2} = \sigma \iint \rho_1(x_2 + \Delta x, y_2 + \Delta y)\rho_2(x_2, y_2)\mathrm{d}x_2\mathrm{d}y_2, \tag{1.14}$$

where ρ_1 and ρ_2 are the normalized transverse particle density functions of the two beams. Integrating Eq. 1.14 in Δx and Δy, the equation becomes

$$\iiiint \rho_1(x_2 + \Delta x, y_2 + \Delta y)\rho_2(x_2, y_2)\mathrm{d}x_2\mathrm{d}y_2 \; \mathrm{d}\Delta x \, \mathrm{d}\Delta y = 1. \tag{1.15}$$

This result can be easily proven by substituting $x_1 = x_2 + \Delta x$ and $y_1 = y_2 + \Delta y$. Then, it is possible to decouple ρ_1 and ρ_2 in two integrals that reduce to unity by definition. Finally, by using Eq. 1.14 and Eq. 1.15, the so-called Van der Meer expression for σ is

$$\sigma = \iint \frac{\mu(\Delta x, \Delta y)}{N_1 N_2} \mathrm{d}\Delta x \, \mathrm{d}\Delta y. \tag{1.16}$$

It is useful to introduce a new parameter, the specific number of interactions, $\mu_{sp}(\Delta x, \Delta y) = \mu(\Delta x, \Delta y)/N_1 N_2$. Assuming that the beams densities can be factorised into their respective x and y dependent parts, it follows that $\mu_{sp}(\Delta x, \Delta y)$ can be also factorised. This allows to simplify the bidimensional integral into a product of two one-dimensional integrals.

$$\begin{aligned}\sigma = \iint \mu_{sp}(\Delta x, \Delta y)\mathrm{d}\Delta x \, \mathrm{d}\Delta y &= \int \mu^x_{sp}(\Delta x)\mathrm{d}\Delta x \int \mu^y_{sp}(\Delta y)\mathrm{d}\Delta y \frac{\mu^x_{sp}(\Delta x_0)\mu^y_{sp}(\Delta y_0)}{\mu^x_{sp}(\Delta x_0)\mu^y_{sp}(\Delta y_0)} \\ &= \frac{\int \mu_{sp}(\Delta x, \Delta y_0)\mathrm{d}\Delta x \int \mu_{sp}(\Delta x_0, \Delta y)\mathrm{d}\Delta y}{\mu_{sp}(\Delta x_0, \Delta y_0)},\end{aligned} \tag{1.17}$$

where Δx_0 and Δy_0 are reference points. The two integrals can be measured in two one-dimensional scans over Δx at fixed Δy_0 and vice versa. Though the formula is valid for any given point (Δx_0, Δy_0), it is convenient to choose (Δx_0, Δy_0) not too far from the point of maximum luminosity in order to collect sufficient statistics of interactions. It is important to underline the fact that in Eq. 1.17 μ_{sp} is used and not μ and $N_1 N_2$

separately. This means that μ and the number of particles can vary arbitrarily during the scan as long as they vary proportionally. This is likely to happen due to the gradual decrease of beam currents with time.

This approach is valid only under the approximation of x-y independence. At LHC, this approximation is good but not perfect. In order to increase the precision, two-dimensional scans over the central region have been performed since 2017 when it was first pioneered at LHCb. Scans performed over the only central region are relatively fast but allow to evaluate roughly 90% of the integral in Eq. 1.16.

Chapter 2

LHC

Large Hadron Collider (LHC) is currently the largest particle accelerator on Earth. It has a circumference of 27 km and it is designed to collide protons up to 14 TeV center of mass energy at up to $10^{34} cm^{-2} s^{-1}$ instantaneous luminosity. It is located at the final stage of the CERN's accelerator complex, receiving bunches of protons of 450 GeV from the Super Proton Synchrotron (SPS). Here we have two rings in which the protons travel in bunches of 10^{11} particles in opposite directions. There are 4 crossings between the two rings where the 4 major experiments are located: ATLAS, CMS, ALICE and LHCb. Fig. 2.1 shows a representation of the complex.

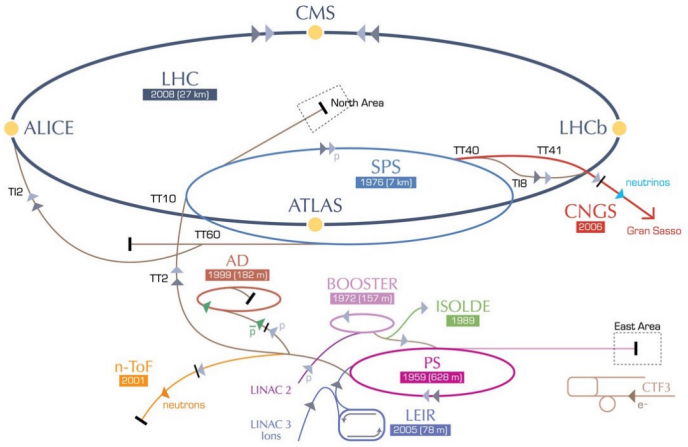

Figure 2.1: *CERN's accelerator complex [3].*

2.1 LHCb

Large Hadron Collider beauty is one of the 4 major experiment at LHC [4]. Its primary goal is to look for indirect evidence of new physics in CP violation and rare decays of beauty and charm hadrons. Compared to other experiments at LHC, it operated at smaller luminosity around $10^{32} cm^{-2} s^{-1}$ during Run 1 and Run 2. The LHCb detector is a single-arm forward spectrometer. It covers an angular region between 10 and 300 mrad in the horizontal (bending) plane and between 10 and 250 mrad in the vertical plane. Its geometrical acceptance is motivated by the fact that in pp collisions, both $b\bar{b}$ and $c\bar{c}$ pairs are produced with a preferentially small polar angle distribution. A schematic cross section of the detector and its components is shown in Fig. 2.2.

The main features of the detector, required in order to carry out its physics program, are the following:

- An efficient, robust and flexible trigger in order to cope with the harsh hadronic environment. The trigger must be sensitive to many different final states.
- An excellent precision in the reconstruction of the interaction vertices and of the B and D hadrons decay vertices. Indeed, to measure neutral mesons oscillation and CP violation it is fundamental to have a suitable proper-time resolution.
- A good identification of protons, kaons and pions in order to cleanly reconstruct many hadronic B and D meson decay final states.
- A data acquisition system with high bandwidth and powerful online data processing capability, needed to optimise the data taking.

A brief description of the LHCb detector during Run 1 and Run 2 follows. We can divide the components of the detector in two different systems:

- Tracking system. It is composed by the VErtex LOcator (VELO) surrounding the interaction point and four tracking stations. The first one, the Trigger Tracker (TT), is positioned upstream the magnet while the other 3 (T1-T3) are positioned downstream.
- Particle identification system. It is composed by two Ring Imaging CHerenkov (RICH1 and RICH2), positioned upstream and downstream the magnet, two calorimeters (ECAL and HCAL) and 5 muon detection stations (M1-M5). Two auxiliaries detector upstream the calorimeters are also present (SPD and PS).

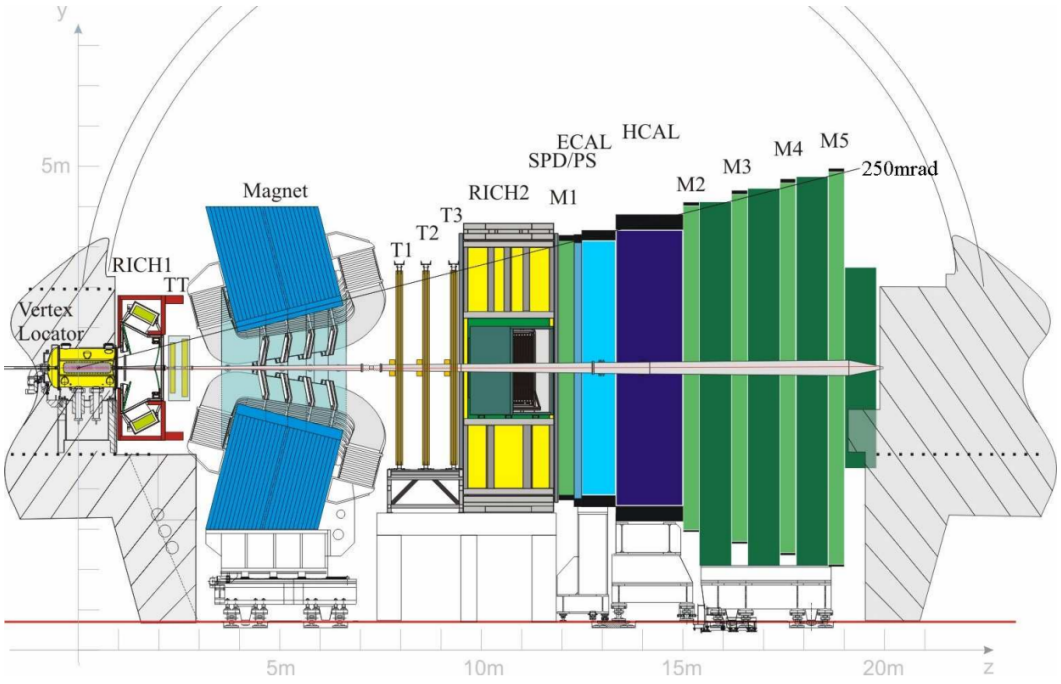

Figure 2.2: *LHCb detector [4].*

2.2 Tracking system

The tracking system is devoted to identify the interaction vertices, reconstruct the trajectories of charged particles and measure their momentum exploiting a magnetic field to bend them.

2.2.1 Vertex locator

The VELO is the closest component of the detector to the interaction point. Its purpose is to precisely measure the position of primary and secondary vertices. It is composed by 21 silicon modules each one divided in two halves so that the VELO has two different configurations:

- **Open**: during the beam stabilization phase. The two halves are separated by 6 cm.
- **Closed**: during data taking phase. The two halves slightly "overlap" so that no tracks are lost

The modules are composed of two planes of 220 µm thick silicon micro-strip sensors able to measure the distance from the beam R and the polar angle ϕ of hits generated by the

ionizing particles that cross the VELO. This structure is represented in Fig. 2.3.

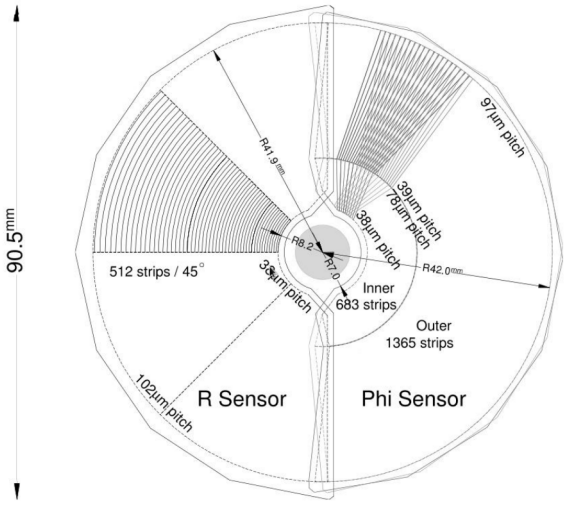

Figure 2.3: *R and ϕ sensors [4].*

2.2.2 Trigger tracker and tracking stations

The TT task is to provide reference segments used to combine the track reconstructed in the tracking stations with those reconstructed in the VELO, in order to improve the momentum and coordinate resolution. The system is composed by 4 stations composed by silicon microstrips. In the first and fourth stations the strips are parallel to the vertical plane, while in the second and in the third stations they are tilted respectively by $+5°$ and $-5°$. This is done to improve the precision of the track reconstruction. Downstream the magnet, other 3 tracking stations are placed. Each is composed by an Inner Tracker (IT) and an Outer Tracker (OT). The inner tracker is closer to the beam and it is composed by 4 stations of silicon microstrips arranged like the ones of the TT. The OT has a similar configuration of 4 layers but it does not use silicon microstrips. In this area, particle density is significantly lower than in the IT so drift tubes are used. This technology is not as efficient as silicon microstrips but it's much cheaper.

2.2.3 Magnet

All modern experiments measure particle momenta through their curvature in a given magnetic field. For this reason, the LHCb detector is provided with a warm magnet dipole. The magnet is formed by two coils placed with a small angle with respect to the beam axis, to increase the opening window with z in order to follow the acceptance of the LHCb detector. Among the main LHC experiments, the LHCb detector has a

unique feature consisting in the possibility to reverse the polarity of the magnetic field. This allows a precise control of the left-right asymmetries introduced by the detector.

2.3 Particle identification

2.3.1 RICH detectors

The two RICH detectors exploit the light emitted by particles that travel in a medium faster than light in the same medium. This is called Cherenkov effect. The relation between the Cherenkov photon emission angle θ_c and the refraction index n of the radiator is:

$$\theta_c = \frac{1}{\beta n} \tag{2.1}$$

Where $\beta = v/c$ is the particle speed relative to the speed of light in vacuum. Cherenkov light emission only occurs when the particles exceeds the threshold value of $\beta_c = 1/n$ while each radiator has a maximum emission angle $\theta_c^{max} = arccos(1/n)$. It is evident that for particles approaching the speed of light, the Cherenkov angle will saturate to θ_c^{max} and it is therefore necessary to have different radiators in order to discriminate particles in a wide range of momenta. The RICH1 is optimized for low momentum particles while RICH2 for high momentum particles up to 150 GeV/c. Measuring the photons hit positions, it is then possible to discriminate the various mass hypotheses.

2.3.2 Calorimeters

The calorimeter system is used to identify electrons, photons and events which are hadronic in nature. It consists of a Scintillator Pad Detector (SPD), a Pre-Shower (PS) detector, an Electromagnetic Calorimeter (ECAL) and a Hadronic Calorimeter (HCAL). All the subdetectors making up the calorimeters system are made of segmented scintillators, acting as active material, and light is transported by wavelength shifting fibers and read out by photomultipliers. The SPD is used to discriminate between electrons and photons. By comparing the number of hits in the SPD and PS, it is possible to separate electrons and the background of charged pions from their longitudinal shower dispersion. ECAL measures the enegies of particles with electrical charge while HCAL measures the energies of hadronic showers.

2.3.3 Muon detectors

Muons are minimum ionizing particles traversing all the detector without suffering major energy losses. The muon stations are therefore placed at the end of the detector,

where mainly muons are present, and provide muon identification and standalone track reconstruction and transverse momentum p_T calculation for trigger purposes. One muon station (M1) is placed upstream the calorimeters, providing an improved p_T measurement for the trigger, while the remaining four stations (M2-M5) are placed downstream the calorimeters. Muon stations are made of multiwire proportional chambers, except for the inner part of the M1 station, made of triple-GEM (gas electron multiplier) detectors, which provide better radiation hardness in the presence of high particle fluxes. Each muon station is subdivided into four parts (R1-R4) with increasing segmentation for diminishing distance from the beam pipe, allowing for an equally distributed particle occupancy.

Chapter 3

PLUME

During LHC run 3, the LHCb detector will be subject to a 5 times increase in luminosity compared to Run 1 and Run 2. The detector has been upgraded and requires a new subdetector to determine a precise measurement of luminosity in real-time. This task will be performed by PLUME (Probe for LUminosity MEasurement) [5].

3.1 PLUME elementary detection module

The hodoscope of PLUME is composed by 48 elementary detection modules. The layout of one module is illustrated in Fig. 3.1. The PMT and the divider circuit are fitted inside an aluminium cylindrical shield that protrudes beyond the window in order to also host the quartz tablet. The structure allows the correct centering of the quartz tablet respect to the PMT window and allows space for the entrance of the quartz fibre that brings the light to the front surface of the quartz tablet for the monitoring purposes. A magnetic shield surrounds the PMT in order to remove any eventual remaining effect due to magnetic field at the PLUME position.

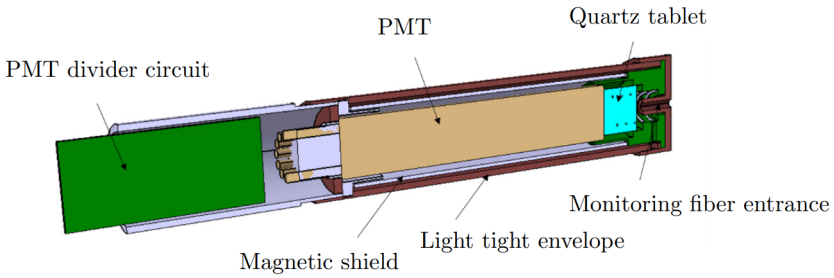

Figure 3.1: *Schematic view of the PLUME elementary detection module [5].*

3.1.1 The R760 photomultipliers

The choice of detector is crucial for the correct operation of the detector. A set of requirements and considerations must be taken into account. First of all a fast signal is required to be well within the minimum distance of 25 ns between two sequential beam crossings in order to avoid spillover and to ensure an efficient readout. The amount of signal from a traversing particle should be significant, so that a potential threshold drift does affect the precision of the luminosity measurement, and well above the instrumental noise. The use of radiation-resistant materials is imposed by the harsh environment. Classical PMTs made with radiation hard materials like metal and quartz have been chosen for PLUME. The selected photomultiplier tube model for PLUME is the R760 PMT produced by HAMAMATSU which is a Head-on type photomultiplier tube with linear-focused dynodes structure composed by 10 steps.

3.1.2 The quartz radiators

The quartz radiator is fixed in front of the PMT window in order to increase the amount of produced Cherenkov light from the traversing particle. A 5 mm thick quartz tablet is positioned in front of the 1.2 mm thick quartz PMT window. The quartz type for the radiator, SPECTROSIL 2000, has been chosen in order to have a good transmittance for the Cherenkov light spectrum range and to be resistant enough to stand the expected level of radiation in PLUME.

3.2 PLUME detector layout and design

A total of 48 modules are arranged in a projective geometry and form a two-layer hodoscope. The first layer of PMT is positioned at 1680 mm from the nominal interaction point, the second at 1900 mm. The accuracy of the alignment in X and Y will be less than 1 mm. The alignment in Z is less constraining due to the significant extension of luminous region along the beam direction. In each layer, the elementary detectors form a cross around the beam pipe. The detectors are positioned at angles ranging between approximately 5° and 10° from the beam axis. The exact detector angular positions are shown in Fig. 3.2.

Two cross-shaped aluminium structures, placed one behind the other, corresponding to two hodoscope planes, serve to support 24 modules each. The detector arrangement in the mechanical supporting structure is illustrated in Fig. 3.3 with side and beam views.

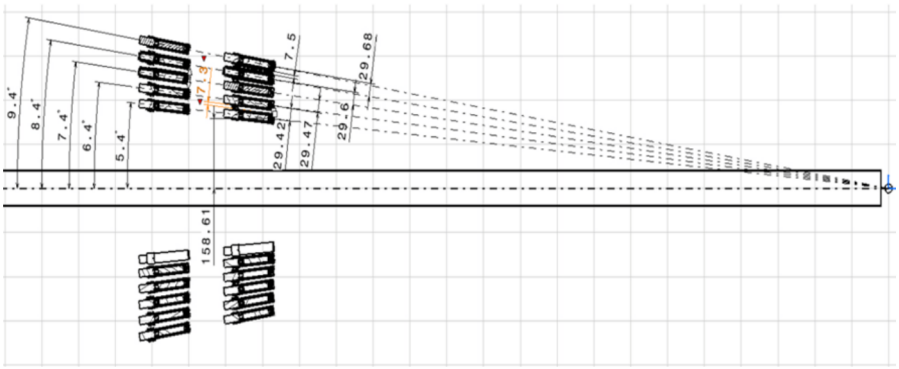

Figure 3.2: *Angular positions of PLUME elementary detectors with respect to the nominal primary pp collision vertex [5].*

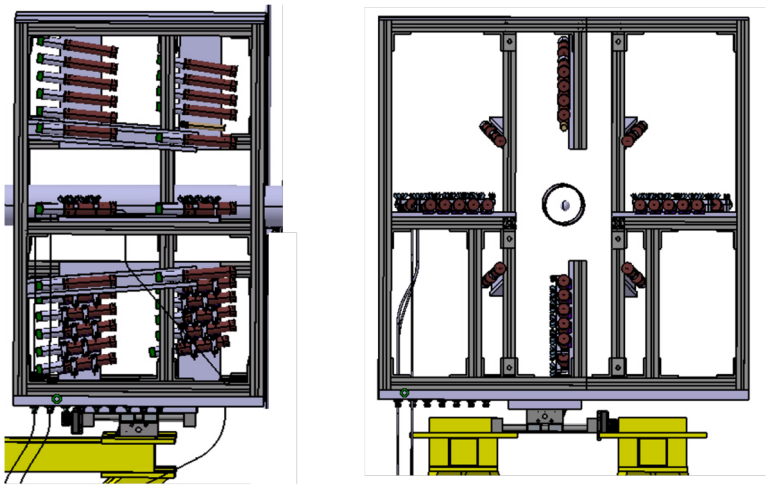

Figure 3.3: *PLUME detector arrangement, (left) side and (right) beam views [5].*

The detector box is divided into A and C side parts and is mechanically protected from outside by a grid, which is common to VELO, SMOG2 (System for Measuring the Overlap with Gas) and PLUME detectors. Grid elements can be removed to access the elementary detectors. The integration of the PLUME detector in LHCb takes into account the neighbouring systems, in particular VELO, SMOG2 and BCM, and the infrastructure of these systems, the beam pipe and the vacuum system.

Chapter 4

Simulation of the expected occupancy and van der Meer scan

To estimate the expected performance of the PLUME detector, a Monte Carlo simulation based on Pythia8 and Geant4 has been developed. The former produces particles in proton-proton collisions at a center-of-mass energy of 13 TeV, with a zero beam crossing angle, including both hard and soft QCD processes. Particles from the Pythia simulation, which will be called primaries in the following, are propagated to the Geant4. Here, the primaries can interact with the simulated structures such as the VELO and RFfoil, originating secondaries. Pythia and Geant are implemented inside GAUSS which is the official simulation tool for LHCb. Physicists at LHCb use a simple code with input parameters and obtain an output file which contains all the data for the simulated particles. Then, the subsequent interaction with the detector has been simulated with a script confronting the trajectories of the particles with the positions of the 48 PMTs.

4.1 The simulated detector

The detector has been simulated by 24 pairs of PMts placed at different angles in respect to the beam line and the interaction point (IP = (0,0,0)) in two planes at $z = -1680$ mm and $z = 1900$ mm. Each PMT has a 5 mm radius and the quartz tablet (in which the Cherenkov photons are produced) is 6.2 mm long. To simulate the interaction, the particles trajectories are reconstructed using the particles origin points and momentum components using the following

$$x = x_0 + (z - z_0)\frac{p_x}{p_z} \qquad y = y_0 + (z - z_0)\frac{p_y}{p_z}, \tag{4.1}$$

where z is the position along the z axis in which we want to evaluate the x and y coordinates. For $z_{min} \leq z \leq z_{max}$, where z_{min} and z_{max} are the two extremes of the

quartz tablet, the trajectory of the particle is evaluated and, if the latter falls inside the volume of the tablets, a detection is registered. During the simulation, only particles with electrical charge have been considered. This is because only these particles can emit photons via Cherenkov effect. In Fig. 4.1 different particle types detected by the simulated position of the PMTs are shown.

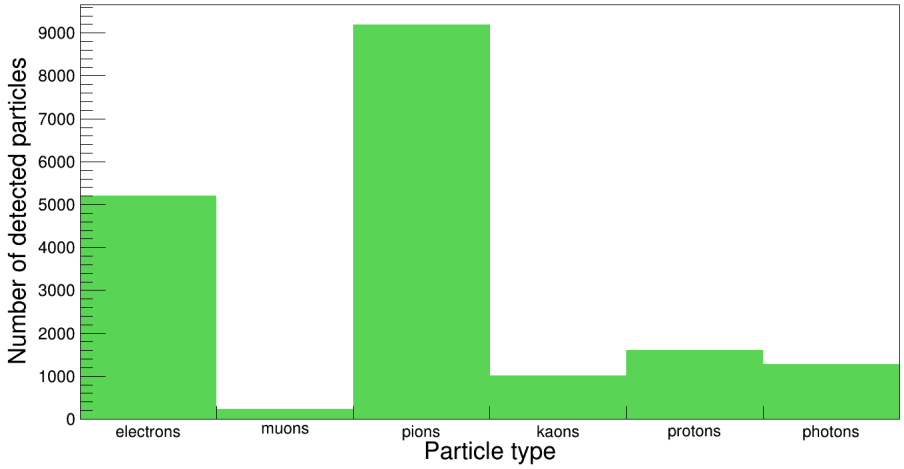

Figure 4.1: *Types of detected particles over about 20000 events. The respective antiparticles have been included in the same bins of the particles. This is because particles and antiparticles where observed in similar rates.*

4.2 Simulated occupancy

The data from the GAUSS simulation is divided into events. Each event simulates a collision between two bunches in which many particles are produced. An event is observed whenever a particle originating from the collision is detected. For a single PMT, the occupancy is the probability of an event to be observed. In Fig. 4.2, the occupancy of the PMTs at different angles is shown and in Tab. 4.1 the data are reported.

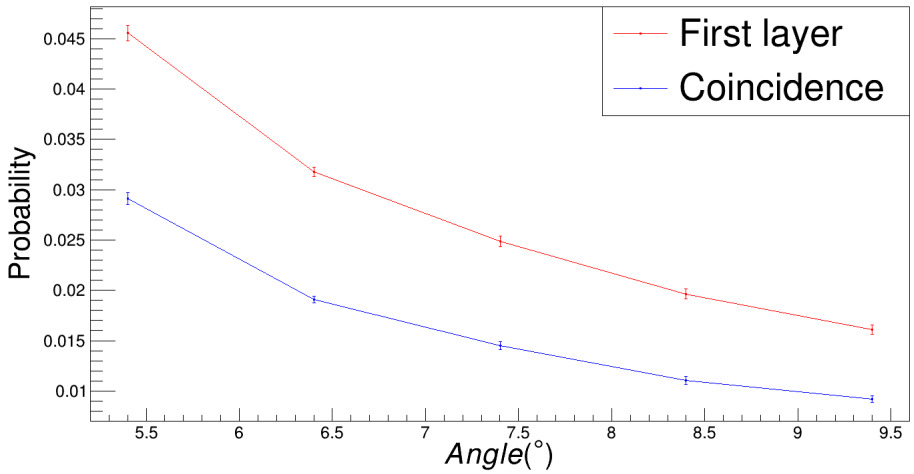

Figure 4.2: *Expected occupancy at different angles. First layer shows occupancy of the PMTs in z = -1680 mm. Coincidence shows the probability of an event to be observed by a pair of projective PMTs.*

angle	occupancy
5.4°	0.0456 ± 0.0015
6.4°	0.0318 ± 0.0013
7.4°	0.0248 ± 0.0011
8.4°	0.0196 ± 0.0010
9.4°	0.0161 ± 0.0009

(a) First layer

angle	occupancy
5.4°	0.0291 ± 0.0012
6.4°	0.0191 ± 0.0010
7.4°	0.0145 ± 0.0009
8.4°	0.0110 ± 0.0007
9.4°	0.0092 ± 0.0003

(b) Coincidence

Table 4.1: *(a) First layer shows occupancy of the PMTs in z = -1680 mm. (b) Coincidence shows the probability of an event to be observed by a pair of projective PMTs.*

The highest value is obtained for the PMTs at 5.4° and it corresponds to about 4.5%. It is possible for a PMT to be hit by more than one Cherenkov photon emitted by a particle during an event, however in most of the cases only one particle causes the PMT to emit a signal. One could note that the relative uncertainty of the PMTs at 6.4° is smaller than the ones of other angles by a factor $1/\sqrt{2}$. That is because in each PMT layer, 4 additional PMTs are not positioned in the cross structure of PLUME but are positioned at 45° from both of the two principal "lines" which form the cross. Those are placed at 6.4° from the beam line resulting in having double the number of PMTs for that angle and, therefore, double the statistics and a more accurate measurement.

It is essential to verify the hypotesis of independence between the different PMTs in a layer. If not confirmed, this would lead to overestimating luminosity during an experiment because of different PMTs hit by a single particle. In order to do so, we will firstly evaluate the average occupancy of the first layer of PMTs, which is ∼0.028, from the reported data in Tab 4.1. By multiplying this result with the number of PMTs/layer, *i.e.* 24, one gets a value of ~ 0.7. Secondly, we can evaluate the average number of fired channels in the first layer of PMTs from the data in Tab. 4.2 (a) which is ~ 0.7. The consistency between those two different evaluations verifies our hypotesis. In Fig. 4.3 the number of fired channels in the first layer and the logical combination (AND, OR) from pairs of projective PMTs is shown and the data are presented in Tab. 4.2.

n° of fired channels	probability
0	0.4971 ± 0.0050
1	0.3339 ± 0.0041
2	0.1200 ± 0.0025
3	0.0382 ± 0.0014
4	0.0088 ± 0.0007
5	0.0017 ± 0.0003
6	0.0003 ± 0.0001

(a) First layer only

n° of fired channels	probability
0	0.6462 ± 0.0057
1	0.2750 ± 0.0037
2	0.0647 ± 0.0018
3	0.0124 ± 0.0008
4	0.0013 ± 0.0003
5	0.0002 ± 0.0001
6	0.0001 ± 0.0001

(b) AND

n° of fired channels	probability
0	0.4477 ± 0.0047
1	0.3413 ± 0.0042
2	0.1436 ± 0.0027
3	0.0489 ± 0.0016
4	0.0142 ± 0.0009
5	0.0035 ± 0.0004
6	0.0006 ± 0.0002
7	0.0001 ± 0.0001

(c) OR

Table 4.2: *Number of fired channels in the PLUME detector and relative probability. The channel is either a PMT in the first layer at z = 1680 mm (first layer only) or the logical combination(AND, OR) with the respective PMT in the second layer at z = 1900 mm.*

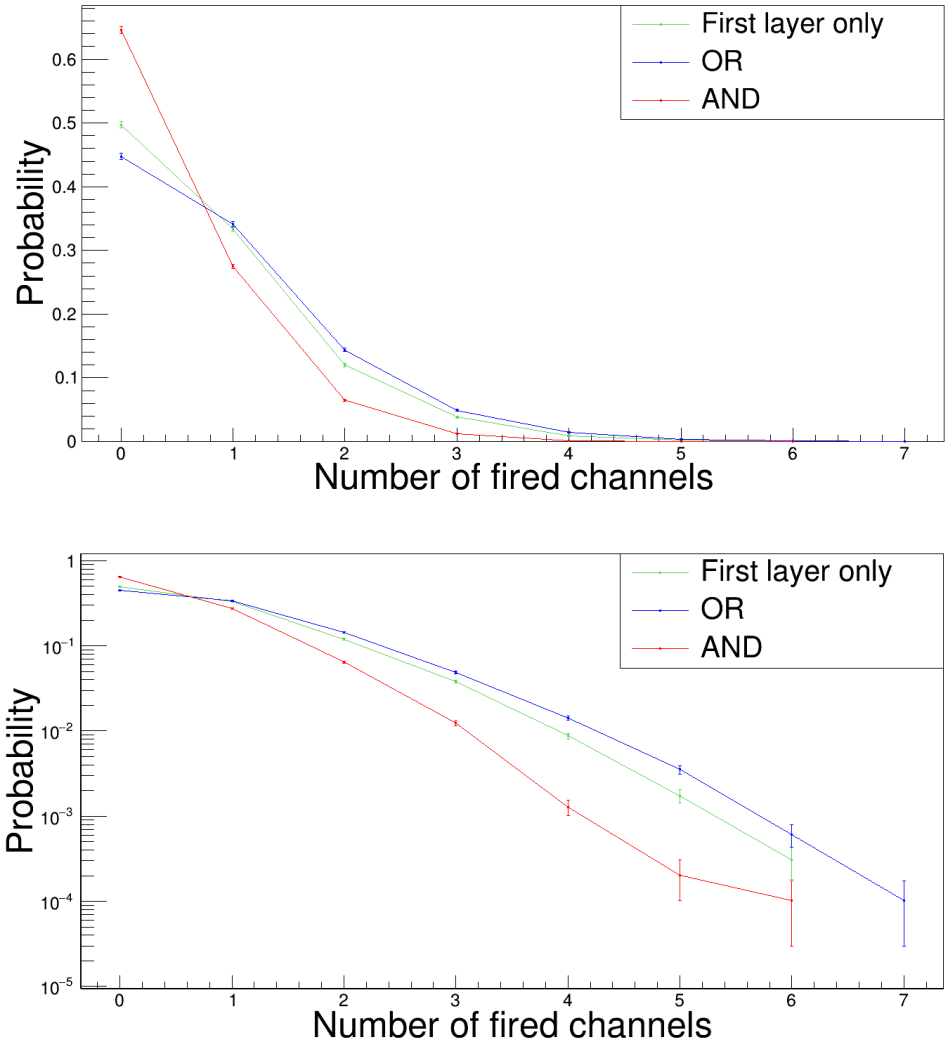

Figure 4.3: *Number of fired channels in the PLUME detector. The channel is either a PMT in the first layer at z = -1680 mm (first layer only) or the logical combination(AND, OR) with the respective PMT in the second layer at z = -1900 mm. Distributions are shown in (up) linear and (down) logarithmic scale.*

4.3 Van der Meer scan with the Run 3 collisions

Recalling Eq. 1.16 and Eq. 1.17, one must conclude that to evaluate the cross section σ in a Van der Meer scan, one must first know the specific number of interactions $\mu_{sp}(\Delta x, \Delta y)$ that are obtained from the measurements of the number of interactions per bunch-crossing $\mu(\Delta x, \Delta y)$ and the populations of the colliding bunches N_1 and N_2.

During time intervals of 15 seconds, the beams are displaced at constant $\Delta x'$ and $\Delta y'$. Several measurements of μ and $N_{1,2}$ and an average value of $\mu_{sp}(\Delta x', \Delta y')$ is considered. The procedure is repeated for different values of Δx and Δy. The value of μ_{sp} is evaluated using the so called logZero method. Assuming Poisson statistics, the probability of having zero collisions is $P(0) = e^{-\mu}$, then

$$\mu = -\log P(0) = -\log \frac{N_0}{N} - \frac{1}{2}(\frac{1}{N_0} - \frac{1}{N}), \tag{4.2}$$

where N is number of expected events (collisions) and N_0 the number of empty events. The definition of empty event is detector dependent. In PLUME, an empty event is defined as an event with all the PMT responses below a certain threshold. The second term in Eq. 4.2 is a correction due to the non-linearity of the logarithm. In fact, what should be consider is the average of number of empty events, $n_0 = \langle N_0 \rangle$ which follows a Binomial distribution, *i.e.*

$$\frac{n_0}{N} = \langle \frac{N_0}{N} \rangle = \langle e^{-\mu} \rangle, \tag{4.3}$$

and applying the logarithm, it becomes

$$\langle \log \frac{N_0}{N} \rangle = \langle \log e^{-\mu} \rangle = \langle -\mu \rangle = -\mu. \tag{4.4}$$

The correct estimation of μ is

$$\mu = -\langle \log \frac{N_0}{N} \rangle = -\langle \log \frac{n_0}{N} \rangle + \langle \log \frac{n_0}{N_0} \rangle = -\langle \log \frac{n_0}{N} \rangle + \langle \log(1 + \frac{n_0 - N_0}{N_0}) \rangle$$

where applying Taylor expansion and considering $-\log \frac{N_0}{N}$ the best estimation of $-\langle \log \frac{n_0}{N} \rangle$, the previous expression becomes

$$\mu \approx -\log \frac{N_0}{N} + \langle \frac{n_0 - N_0}{N_0} \rangle - \langle \frac{(n_0 - N_0)^2}{2N_0^2} \rangle. \tag{4.5}$$

The second term of the previous expression vanish, while the third term corresponds to a variance of the Binomial distribution $NP(0)(1 - P(0)) = N_0(1 - N_0/N)$, namely

$$\langle \frac{(n_0 - N_0)^2}{2N_0^2} \rangle = \frac{N_0(1 - N_0/N)}{2N_0^2} = \frac{1}{2}(\frac{1}{N_0} - \frac{1}{N}), \tag{4.6}$$

hence the best estimation of μ is

$$\mu \approx -\log \frac{N_0}{N} - \frac{1}{2}(\frac{1}{N_0} - \frac{1}{N}). \tag{4.7}$$

The first Van der Meer scan for PLUME was done the 5th of May of 2022 with proton-proton collisions data collected at a center-of-mass energy of 900 GeV, significantly lower

than the maximum energy achievable at LHC. In one hour and 30 minutes, 360 measurements of μ_{sp} were performed, corresponding to one-dimensional and two-dimensional scans. The one-dimensional scan consists in 37 variations in the x plane with 37 measurements of $\mu_{sp}(\Delta x, \Delta y_0)$, and 37 additional variations in the y plane with 37 measurements of $\mu_{sp}(\Delta x_0, \Delta y)$. In Fig. 4.4, the values of μ_{sp} for the x- and y-scan are shown.

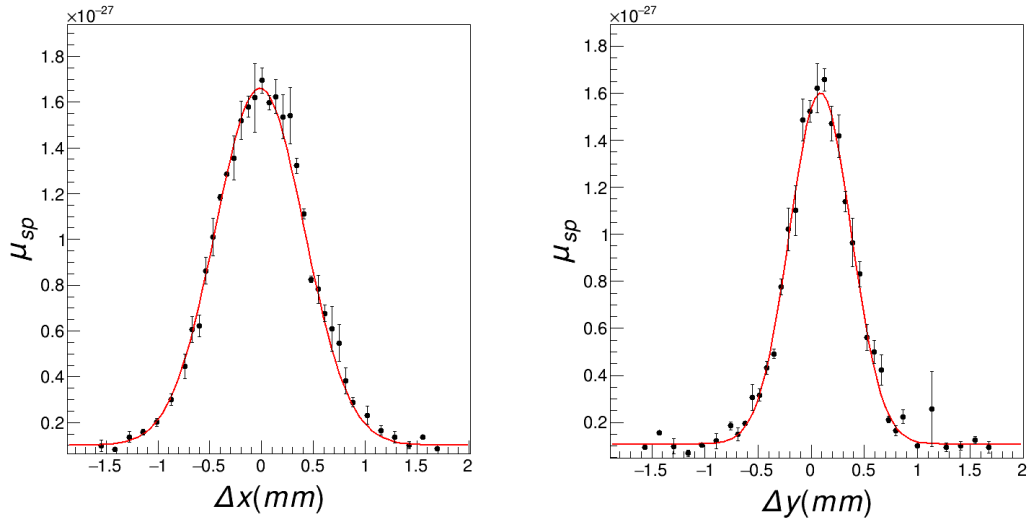

Figure 4.4: *One-dimensional scan (left) over Δx with Δy_0 fixed and (right) over Δy with Δx_0 fixed. Both graphs are fitted assuming a gaussian distribution with a common background.*

From the scans, it is possible to observe a Gaussian profile of μ_{sp} with a small background noise due to beam-gas interactions, visible in the tails. The profiles are fitted with a Guassian function and the results are reported in Tab. 4.3. It is worth to note that σ_x and σ_y can be defined as the beam sizes along x and y axes, respectively.

Parameter	Value
Background noise	$(1.01 \pm 0.04)10^{-28}$
A_x	$(1.561 \pm 0.014)10^{-27}$
μ_x(mm)	$(-1.7 \pm 0.3)10^{-2}$
σ_x(mm)	0.429 ± 0.005

(a) X-scan

Parameter	Value
Background noise	$(1.08 \pm 0.03)10^{-28}$
A_y	$(1.49 \pm 0.03)10^{-27}$
$\mu_y(mm)$	$(8.7 \pm 0.4)10^{-2}$
σ_y(mm)	0.290 ± 0.003

(b) Y-scan

Table 4.3: *Parameters obtained from the fit to the distributions shown in Fig. 4.4. A_i, μ_i and σ_i are the height, mean and standard deviation of a Gaussian function in i=x,y respectively.*

In the scan, the fixed points are, $\Delta x_0 \approx 0.0360$ mm and $\Delta y_0 \approx 0.0275$ mm. By measuring $\mu_{sp}(\Delta x_0, \Delta y_0) = (1.59 \pm 0.08) \times 10^{-27}$, we can finally evaluate Eq. 1.17, with the assumption of Gaussian Δx and Δy profiles

$$\int_{-\infty}^{\infty} A e^{-\frac{(x-\mu)^2}{2\sigma^2}} \mathrm{d}x = A\sigma\sqrt{2\pi}. \tag{4.8}$$

This leads to Eq. 1.17 to be

$$\sigma = \frac{2\pi A_x A_y \sigma_x \sigma_y}{\mu_{sp}(\Delta y_0, \Delta y_0)}. \tag{4.9}$$

From Eq. 4.9, it is possibe to obtain an estimation for the cross section corresponding to $\sigma_{1Da} = (1.14 \pm 0.11)$ mb. During the two-dimensional scan, μ_{sp} is measured over a much more extended two-dimensional region. This allows to increase the number of points for the 1D measurement of the cross section, as shown in Fig. 4.5. The result of the corresponding fit are reported in Tab. 4.4. The corrisponding value of the cross section is $\sigma_{1Db} = (1.13 \pm 0.10)$ mb, in agreement with the previous one.

Parameter	Value
Background noise	$(1.02 \pm 0.04)10^{-28}$
A_x	$(1.583 \pm 0.011)10^{-27}$
μ_x(mm)	$(-1.1 \pm 0.2)10^{-2}$
σ_x(mm)	0.423 ± 0.004

(a) x-scan

Parameter	Value
Background noise	$(1.08 \pm 0.03)10^{-28}$
A_y	$(1.490 \pm 0.016)10^{-27}$
μ_y(mm)	$(7.8 \pm 0.3)10^{-2}$
σ_y(mm)	0.288 ± 0.003

(b) y-scan

Table 4.4: *Parameters obtained by the fit in Fig. 4.5.*

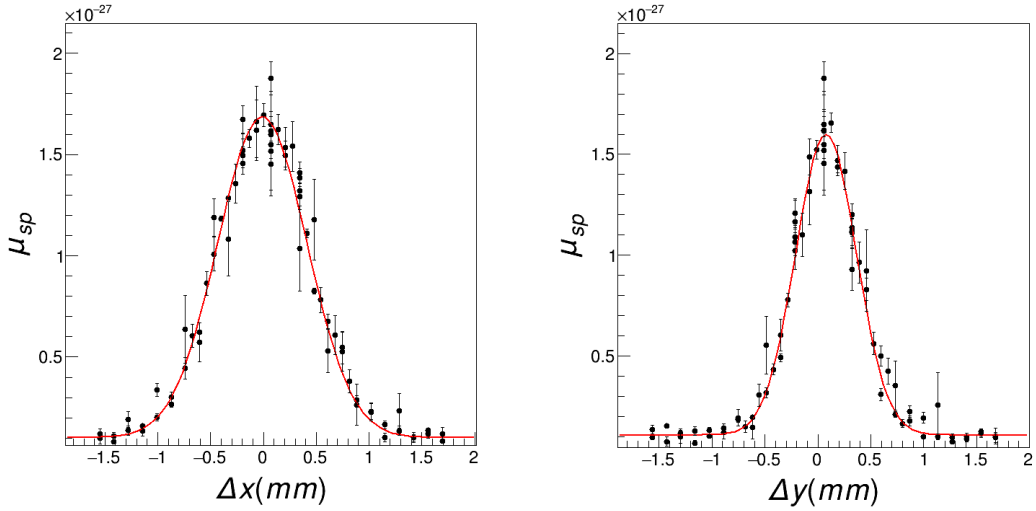

Figure 4.5: *One-dimensional scan with additional points from the two-dimensional scan. The points added to (left)the x-scan have the same fixed Δy_0 and the points added to (right) the y-scan have the same fixed Δx_0. The graphs are fitted as in Fig. 4.4.*

It is possible also to measure the σ from the two-dimensional scan. In Fig. 4.6, the corresponding measurements are depicted on a 3D graph. Assuming that the observed distribution is a product of two uncorrelated Gaussian functions, it is possible to use a bi-dimensional Gaussian to fit the data. The value of the parameters obtained from the fit are reported in Tab. 4.5. Similarly to the 1D case, it possible to obtain a measurement of the cross section $\sigma_{2D} = (1.20 \pm 0.02)$ mb.

Parameter	Value
Background noise	$(1.215 \pm 0.013)10^{-28}$
A	$(1.503 \pm 0.006)10^{-27}$
μ_x(mm)	$(-2.20 \pm 0.17)10^{-2}$
σ_x(mm)	0.4330 ± 0.0019
μ_y(mm)	$(7.63 \pm 0.14)10^{-2}$
σ_y(mm)	0.2959 ± 0.0014

Table 4.5: *Parameters obtained by fitting the data from Fig. 4.5 with a bidimensional gaussian function with an Amplitude A, mean values μ_x and μ_y, and standard deviations σ_x and σ_y.*

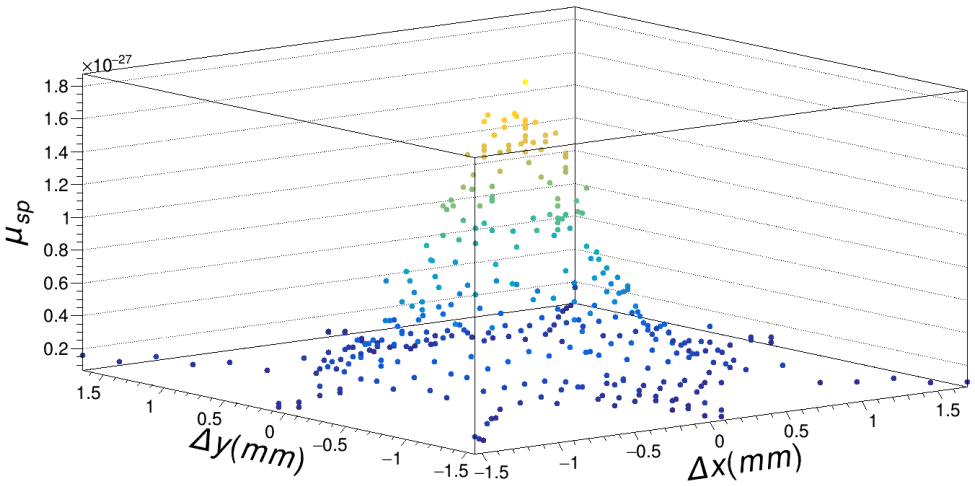

Figure 4.6: *Two-dimensional scan. Points from the previous one-dimensional scans have been added.*

Conclusions

In this thesis, an analysis aiming at evaluating the expected occupancy of the PLUME detector is presented. The data sample used is based on simulated data with GAUSS. A coincidence is most likely caused by a single primary particle originating near the collision point and hitting a pair of projective PMTs of the PLUME detector. The probability of two different secondaries to hit the two PMTs is in general very low. In this way, knowing the ratio between the first layer and coincidence occupancy, it is possible to determine the ratio between particles coming from the collision point and particles originating from collisions with the detector material. In PLUME, the ratio is roughly 3:2, suggesting that 2 out of 3 detected particles are produced in the interaction point.

In addition to this study, it also presented an analysis based on the first Van der Meer scan performed at LHC during the RUN 3. Measurements of visible cross sections have been obtained, namely

$$\begin{aligned} \sigma_{1Da} &= (1.14 \pm 0.11)\,\text{mb}, \\ \sigma_{1Db} &= (1.13 \pm 0.10)\,\text{mb}, \\ \sigma_{2D} &= (1.20 \pm 0.02)\,\text{mb}, \end{aligned}$$

where the labels $1D$ and $2D$ correspond to one-dimensional and two-dimensional beam scans. This result represents the first calibration of the PLUME detector and allows to provide measurements of luminosity to LHC since the beginning the RUN 3.

Bibliography

[1] Werner Herr and B Muratori. "Concept of luminosity". In: (2006). DOI: 10.5170/CERN-2006-002.361. URL: http://cds.cern.ch/record/941318.

[2] Vladislav Balagura. "Van der Meer scan luminosity measurement and beam–beam correction". In: *The European Physical Journal C* 81.1 (Jan. 2021). DOI: 10.1140/epjc/s10052-021-08837-y. URL: https://doi.org/10.1140%2Fepjc%2Fs10052-021-08837-y.

[3] Christiane Lefèvre. "The CERN accelerator complex. Complexe des accélérateurs du CERN". 2008. URL: http://cds.cern.ch/record/1260465.

[4] TL Collaboration et al. "The LHCb detector at the LHC". In: *Journal of instrumentation* 3.08 (2008), S08005–S08005.

[5] CERN (Meyrin) LHCb Collaboration. *LHCb PLUME: Probe for LUminosity MEasurement*. Tech. rep. Geneva: CERN, 2021. DOI: 10.17181/CERN.WLU0.M37F. URL: https://cds.cern.ch/record/2750034.